Supplemental Information

Multiconfigurational non-adiabatic molecular dynamics towards photochemical-N_2-extrusion reactions in borodiazenes

Christian Salguero and Steven A. Lopez*

Department of Chemistry and Chemical Biology, Northeastern University, Boston, Massachusetts, 02115, United States

*Corresponding author: s.lopez@northeastern.edu

Active Space Selection

We included all orbitals involved in the proposed denitrogenation reaction of **bd** in the active space. We selected an active space containing twelve electrons distributed over eleven orbitals: six occupied orbitals—comprising 2 n_N, 1 σ_{CN}, 1 n_N (σ_{CN}), 1 n_N (σ_{NN}), and 1 π_{NN}—and five virtual orbitals, including a $2p_B$, 1 π^*_{NN}, 2 σ^*_{CN}, and 1 σ^*_{NN}. (Figure S1). We optimized a minimum structure on the S_0-surface, and compared the vertical excitation energies obtained from our wavefunction methods (SA5-CASSCF(8,7)/cc-pVDZ and SA5-CASPT2(12,11)/cc-pVDZ//SA5-CASSCF(12,11)/cc-pVDZ) with the vertical excitation values obtained from TD-DFT (CAM-B3LYP/cc-pVDZ and ωB97X-D/cc-pVDZ); matching vertical excitation energies and nature of transitions indicated that the CAS(12,11) is accurately capturing the electronic structure of **bd** on the S_0-surface.

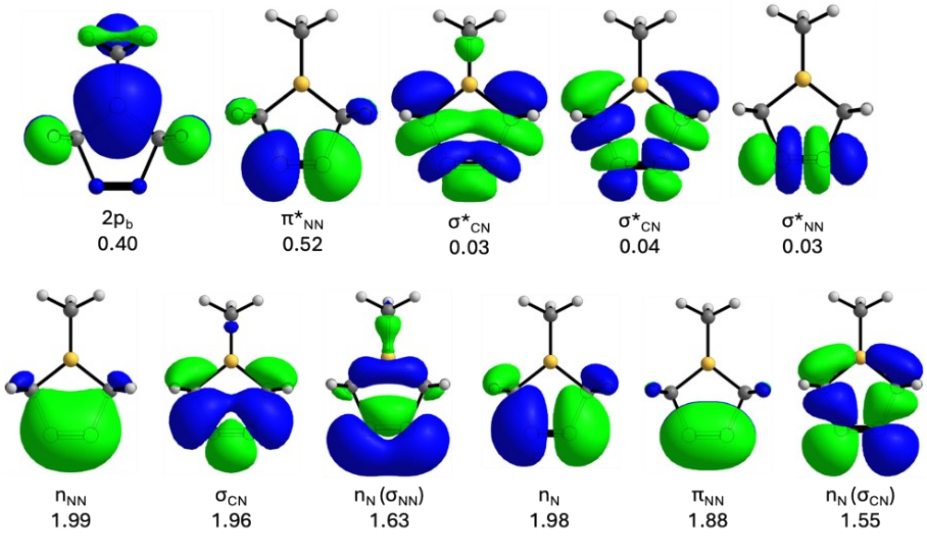

Figure S1. CASSCF(12,11) active space for **bd,** consisting of 12 electrons distributed within 11 orbitals. The 11 orbitals consist of 6 occupied orbitals— 2 n_N, 1 σ_{CN}, 1 n_N (σ_{CN}), 1 n_N (σ_{NN}), and 1 π_{NN}—and 5 virtual orbitals, which include 1 $2p_B$, 1 π^*_{NN}, 2 σ^*_{CN}, and 1 σ^*_{NN}. We listed the average electron occupancy of each orbital below its orbital. An isosurface value of 0.03 was used for all orbital images.

Consequently, we employed SA5-CASSCF(12,11)/cc-pVDZ to study **bd** on both S_1 and S_0 surfaces; we optimized the lowest energy structures on these surfaces, performed vibrational analyses to confirm stationary points, predicted the absorption spectra, and calculated a minimum energy path using SA5-CASSCF(12,11) with the cc-pVDZ basis set. We employed complete-active-space second-order perturbation theory (SA5-CASPT2(12,11)/cc-pVDZ) to account for dynamic correlations at static structures (*e.g.,* **bd-S_0** and **bd-S_1**) and intermediate structures (*e.g.,* **bd-MEP-1** to **bd-MEP-8**). We applied multistate complete-active-space second-order perturbation theory to predict the absorption spectra (Figure 5).

Excited state lifetime

To determine the excited-state lifetime of borodiazene, we monitored the population of the excited state across our ensemble of trajectories and presented the data in Figure S1.

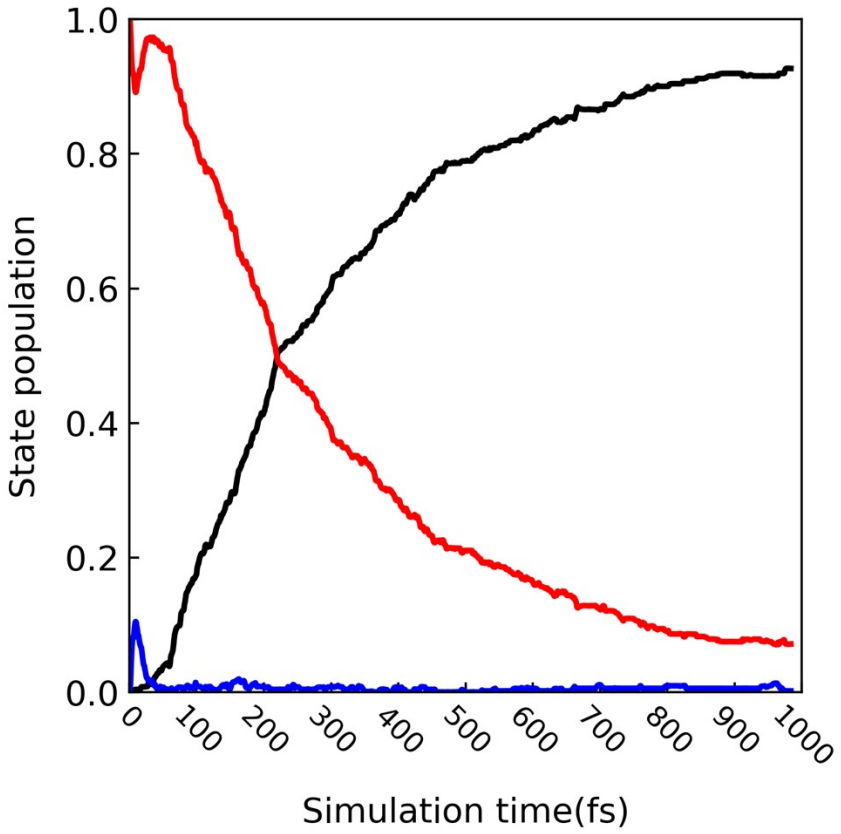

Figure S2. Population map of **bd** over time in picoseconds (ps) derived from QM-NAMD trajectories propagated using SA5-CASSCF(12,11)/cc-pVDZ quantum mechanical calculations. The red line denotes the S_1 population, the blue line denotes the S_2 population, and the black line indicates the S_0 population.

We launched all QM-NAMD trajectories from the S_1 surface. As such, we observe that 100% of trajectories are in the S_1 state at time step 0. We observe an increase in the S_2 population within the first 50 fs. We attribute this increase in the S_2 state population to the near-degeneracy between S_2 and S_1 surfaces at the Franck-Condon region. The excited state half-life for **bd** was 221 fs; the corresponding time constant was 318 fs.

Orbital Overlap

To assess whether **bd** has an accessible excitation wavelength, we used range-separated functionals, specifically ωB97X-D and CAM-B3LYP-GD3(BJ), along with the cc-pVDZ basis set to determine the vertical excitation energies of the ground-state-optimized borodiazene, **bd-S$_0$**. To predict an absorption spectrum, we performed MS-CASPT2(12,11)/cc-PVDZ//SA5-CASSCF(12,11)/cc-pVDZ single-point energy calculations on 500 Wigner-sampled geometries of **bd-S$_0$**; the results were assembled into the spectrum shown in Figure 3 of the main paper. We observed that Figure 3 had three distinct peaks, corresponding to the S_0-S_1, S_2, and S_4 electronic transitions. Both single-reference and multiconfigurational methods confirmed that the $S_0 \rightarrow S_1$ ($n_N \rightarrow \pi^*_{NN}$) transition, although spectroscopically forbidden, is the bright state of **bd** and can be excited using standard experimental light sources. We observed in Figure 3 that the $S_0 \rightarrow S_3$ peak was significantly smaller than those of the other electronic transitions (*i.e.,* $S_0 \rightarrow Sn$, n=1,2,4). Like the $S_0 \rightarrow S_1$ transition, the $S_0 \rightarrow S_3$ also involved a ($n_N \rightarrow \pi^*_{NN}$) transition, which is spectroscopically forbidden. To understand the differences between the absorption peaks in the predicted spectrum, we visualized the orbitals involved in these transitions. The orbital transitions are detailed in Figure S3.

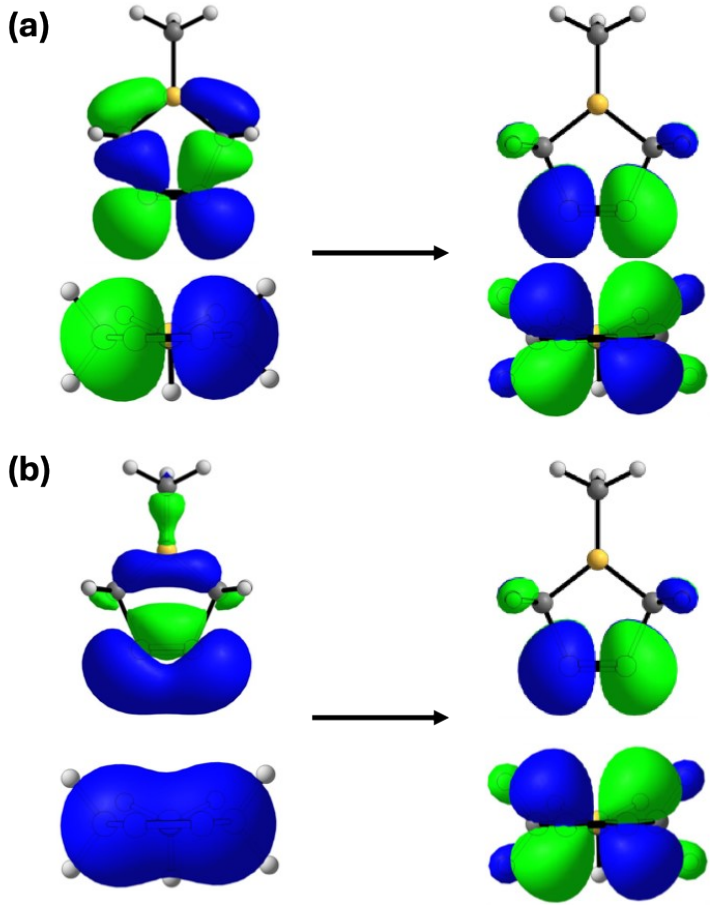

Figure S3. Nature of transitions for (a) S_0 to S_1 ($n_N \rightarrow \pi^*_{NN}$) and (b) S_0 to S_3 ($n_N \rightarrow \pi^*_{NN}$) excitation at the ground-state optimized geometry, **bd-S$_0$**. The isosurface value was uniformly set to 0.03 across all images.

In Figure S3, we visualized the molecular orbital involved in the $S_0 \rightarrow S_1$ ($n_N \rightarrow \pi^*_{NN}$) and $S_0 \rightarrow S_3$ ($n_N \rightarrow \pi^*_{NN}$) vertical excitations (Figure S3a and b). We found that the S_0-to-S_1 transition involves the out-of-phase nonbonding nitrogen orbital, n_{N-}, while the S_0-to-S_3 transition involves the in-phase nonbonding nitrogen orbital, n_{N+}. We hypothesize that this variation in orbital symmetry, whether n_{N-} or n_{N+}, results in the observed differences in transition dipole moments and spectral peaks between the $S_0 \rightarrow S_1$ ($n_N \rightarrow \pi^*_{NN}$) and $S_0 \rightarrow S_3$ ($n_N \rightarrow \pi^*_{NN}$) vertical excitations. An electronic transition must have a nonzero transition dipole moment to possess significant oscillator strength. Given that the dipole operator is an antisymmetric function under inversion, the symmetry of the n_{N+} and π^*_{NN} orbitals leads to an antisymmetric integrand, which corresponds to a zero-transition dipole moment. Conversely, for n_{N-}, the antisymmetry of the orbital, when combined with the asymmetry of the dipole operator, results in a symmetric integrand, thereby producing a nonzero dipole moment. The orbitals shown in Figure S1 and S3 are based on the optimized, ground-state, borodiazene. Geometric distortions, such as those from Wigner sampling, break local symmetry, increase orbital overlaps, and produce a nonzero transition dipole integral, thereby boosting oscillator strength despite the $n_N \rightarrow \pi^*_{NN}$ being spectroscopically forbidden. Although the $S_0 \rightarrow S_1$ ($n_N \rightarrow \pi^*_{NN}$) transition has a nonzero value, it remains a spectroscopically forbidden $n \rightarrow \pi^*$ transition, as indicated by its very small oscillator strength (0.003). Refer to Table 1 of the main manuscript for additional information and discussion.

Minor Denitrogenating Pathways

We identified two minor denitrogenation pathways involving either π_{NN} isomerization or boron pyramidalization. We identified a trajectory that undergoes denitrogenation via the partial *cis*-to-*trans* π_{NN} isomerization pathway, without requiring boron pyramidalization. To enable a direct comparison with Figure 7 of the main paper, we used θ_{BP} and θ_{CNNC} to systematically measure the degree of boron pyramidalization and partial *cis*-to-*trans* π_{NN} isomerization, respectively, along this representative trajectory. 59 trajectories (27%) underwent denitrogenation via the partial π_{NN} isomerization pathway. In Figure S4, we examine a representative trajectory in greater detail.

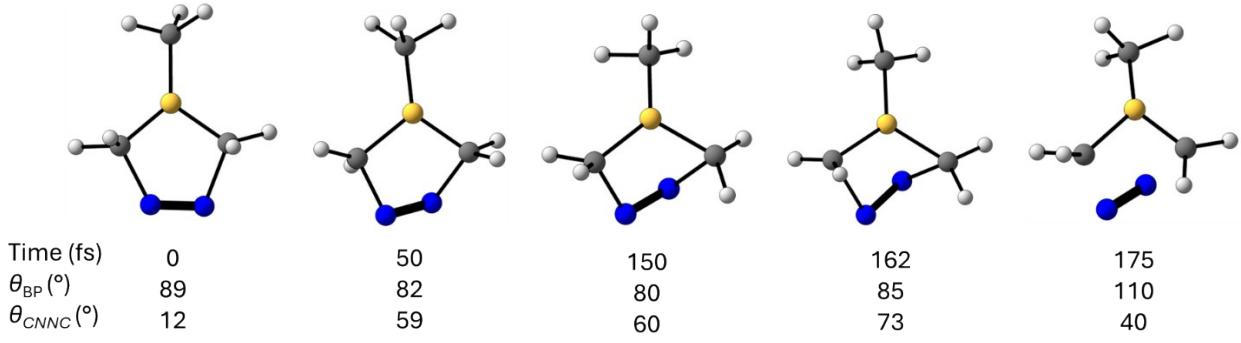

Figure S4. Representative trajectory that undergoes the denitrogenation on the S_1 surface via the *cis*-to-*trans* π_{NN} isomerization pathway.

Figure S4 shows snapshots from a representative trajectory undergoing denitrogenation via the partial *cis*-to-*trans* π_{NN} isomerization pathway. At 0 fs, θ_{BP} is 89°and θ_{CNNC} is 12°. At 50 fs, θ_{BP} is 82°, and θ_{CNNC} is 59°. By 150 fs, θ_{BP} and θ_{CNNC} are 80° and 60°, respectively. At 162, θ_{BP} is 85°, and θ_{CNNC} is 73°. At 175 fs, θ_{BP} is 110°, and θ_{CNNC} is 40°. Between 0 fs and 50 fs, θ_{BP} decreased by 7° while θ_{CNNC} increased by 47°.

The minor change in θ_{BP} and the significant rise in θ_{CNNC} suggest that the $2p_B$ orbital remains unoccupied, and instead, the π^*_{NN} orbital has increased electron occupancy. The θ_{CNNC} value at the 50-fs geometry is not within the *cis*-π_{NN} thresholds, indicating that the π_{NN} underwent a partial *cis*-to-*trans* π_{NN} isomerization during this period. In the next 100fs (50 fs to 150 fs), θ_{BP} decreased by 2°, and θ_{CNNC} increased by 1°, indicating that the geometry remains relatively unchanged during this period. Between 150 fs and 162 fs, θ_{BP} and θ_{CNNC} increased by 5° and 13°, respectively. The θ_{BP} value remains consistent with that of the previous period (50 fs to 150 fs), indicating that the boron underwent minimal geometric changes. The 13° increase in θ_{CNNC} shows that π_{NN} continues to rotate in the same direction as the previous period, leading to increased ring strain in **bd**. At the 162-fs geometry, the trajectory undergoes an S_1/S_0 hop. 13 fs after the S_1/S_0 hop (163-175 fs), the trajectory denitrogenates toward the 1,3-diyl, with θ_{BP} and θ_{CNNC} values of 110° and 40°, respectively. θ_{BP} did not change significantly within this trajectory (±9°) until it fully denitrogenated, indicating no electron occupancy on the $2p_B$ orbital. In contrast, θ_{CNNC} changed substantially (61°) before denitrogenation, demonstrating that the main electronic factor driving the denitrogenation is the excitation to the π^*_{NN} orbital

We also identify a pathway that bypasses partial *cis*-to-*trans* π_{NN} isomerization during denitrogenation and proceeds solely through boron pyramidalization. 37 trajectories (17%) underwent denitrogenation via the boron pyramidalization mechanism. In Figure S5, we investigated a representative trajectory in more detail.

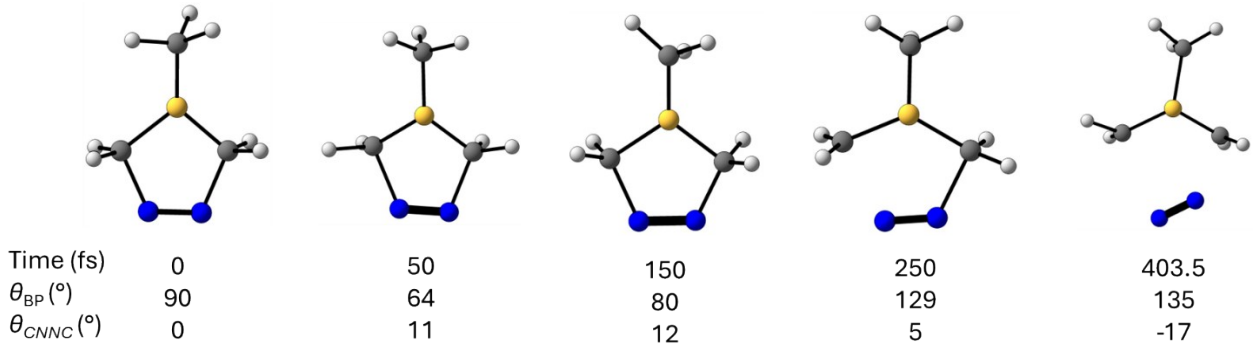

Figure S5. Representative trajectory that undergoes the denitrogenation on the S_1 surface via the boron pyramidalization pathway.

Figure S5 illustrates the denitrogenation mechanism through the boron pyramidalization pathway from a representative trajectory. We report θ_{BP} and θ_{CNNC} to facilitate direct comparison with Figures 7 of the main paper and S4. At 0 fs, θ_{BP} is 90°, while θ_{CNNC} is 0°. By 50 fs, θ_{BP} is 64°, and θ_{CNNC} is 11°. At 150 fs, θ_{BP} is 80°, and θ_{CNNC} is at 12°. At 250 fs, θ_{BP} is 129°, and θ_{CNNC} is 5°. Finally, at 403.5 fs, θ_{BP} is 135°, and θ_{CNNC} is -17°. Between 0 fs and 50 fs, θ_{BP} decreased by 26° while θ_{CNNC} increased by 11°. The slight variation in θ_{CNNC} values implies that the π^*_{NN} orbital remains unoccupied during this period. Conversely, the notable decrease in θ_{BP} reflects an increased occupancy of the $2p_B$ orbital. In the following 100 fs (50 fs to 150 fs), θ_{BP} and θ_{CNNC} increased by 16° and 1°, respectively. The increase in θ_{BP} and the minimal fluctuations in θ_{CNNC} suggest that the dominant electronic configuration during this period has increased $2p_B$ orbital occupancy. From 150 fs to 250 fs, we observed θ_{BP} and θ_{CNNC} increased by 49° and decreased by 7°, respectively. The increase in θ_{BP} past 90° indicates that boron has pyramidilized in the opposite direction relative to the initial pyramidalization (0 fs to 50 fs); there is no significant change in θ_{CNNC}

throughout these snapshots (0-250 fs). We note that the geometric changes in this trajectory align well with those observed between 400 fs and 650 fs in Figure 7 of the main manuscript. At the 250-fs geometry, the θ_{BP} and θ_{CNNC} values (*i.e.,* 125° and 5°) indicate that **bd** has fully adopted the **bd-S$_1$** geometry. The trajectory maintains this geometry until it denitrogenates. At 403.5 fs, the trajectory undergoes an S_1/S_0 hop; it underwent full denitrogenation on the S_1 surface. The θ_{CNNC} is no longer informative, as the π_{NN} has full rotational freedom, whereas the θ_{BP} indicates that the boron remains pyramidalized at this point. This trajectory demonstrates an instance where the full denitrogenation occurs on the S_1 surface. Contrary to the trajectory reported in Figure S4, the trajectory in Figure S5 shows a significant change in θ_{BP} and a relatively small change in θ_{CNNC}. This contrast between the two representative trajectories indicates that the main electronic effect driving denitrogenation in the trajectory in Figure S4 is the increased occupancy of the $2p_B$ orbital rather than the π^*_{NN} orbital.

Minimum Energy Conical Intersection

Based on Figures S4 and S5, we deduce that trajectories undergoing partial *cis*-to-*trans* π_{NN} isomerization before denitrogenation proceed through an S_1/S_0 hopping point, and the denitrogenation is completed on the ground state. Those involving boron pyramidalization before denitrogenation proceed without undergoing an S_1/S_0 hopping point and denitrogenate completely on the S_1 surface. Based on these results, we deduce that the partial *cis*-to-*trans* π_{NN} isomerization is more critical for the denitrogenation than the boron pyramidalization, as it promotes the denitrogenation and the S_1/S_0 hop; although important, this partial *cis*-to-*trans* isomerization is not necessary for the denitrogenation to occur (*i.e.*, denitrogenation occurs from the boron pyramidilized geometry). To assess how the S_1/S_0 hop contributes to the mechanism, we identified a minimum-energy conical intersection for each pathway—boron pyramidalization and partial isomerization—labeled as **bd-MECI-A** and **bd-MECI-B**, respectively.

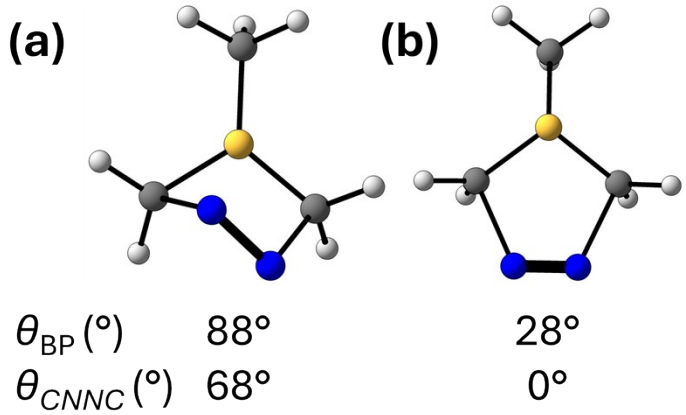

Figure S6. We optimized a minimum energy conical intersection for each mechanistic pathway of photodenitrogenation: **(a)** *cis*-to-*trans* π^*_{NN} isomerization, **bd-MECI-A**, and **(b)** boron pyramidalization, **bd-MECI-B**, using SA5-CASSCF(8,7)/cc-pvdz. Each structure is accompanied by its boron out-of-plane angle, θ_{BP}, and cis-to-trans dihedral angle, θ_{CNNC}.

bd-MECI-A and **bd-MECI-B** have average energies of 3.22 eV and 3.90 eV above **bd-S$_0$**, respectively. These energies indicate that **bd-MECI-A** is 0.68 eV lower in total energy than **bd-MECI-B**. To determine which orbitals are occupied at these MECIs (**bd-MECI-A** and **bd-MECI-B**) and for direct comparison to Figures S4 and S5, we measured θ_{CNNC} and θ_{BP}. In **bd-MECI-A**, θ_{BP} is 88°, and θ_{CNNC} is 68°, while in **bd-MECI-B**, θ_{BP} is 28°, and θ_{CNNC} remains at 0°. These measurements demonstrate that, relative to **bd-S$_0$**, **bd-MECI-A** experienced a 2° change in θ_{BP} and a 68° change in θ_{CNNC}, whereas **bd-MECI-B** had a 62° change in θ_{BP} and no change in θ_{CNNC} (staying at 0°). These geometrical changes indicate that **bd-MECI-A** has

increased electron occupancy on the π^*_{NN}. In contrast, **bd-MECI-B** has increased electron occupancy on the $2p_B$ orbital and is in line with the observed mechanistic pathways. The presence of an MECI between the two mechanistic pathways indicates that they are orthogonal and need not intersect.

To verify whether the MECIs reported in Figure S6 truly represent the ensemble rather than isolated instances, we selected an additional 4 S_1/S_0 hopping-point geometries for further analysis, bringing the total to 6. These included two with partial π_{NN} isomerization, two exhibiting a pyramidalized boron atom, and two with one broken C-N bond (see Figure S7a-c, for representative geometries). All MECIs were optimized using SA5-CASSCF(12,11)/cc-pVDZ. QM-NAMD calculations indicate that the dominant mechanistic pathway involves both boron pyramidalization and partial π_{NN} isomerization, with the latter occurring prior to denitrogenation. Based on this, we hypothesized that MECIs optimized from geometries with π_{NN} isomerization would be lower in energy than those optimized from pyramidalized geometries. The results are summarized in Table S1, with representative initial and final MECI geometries displayed in Figure S7a-c and S7d-f, respectively.

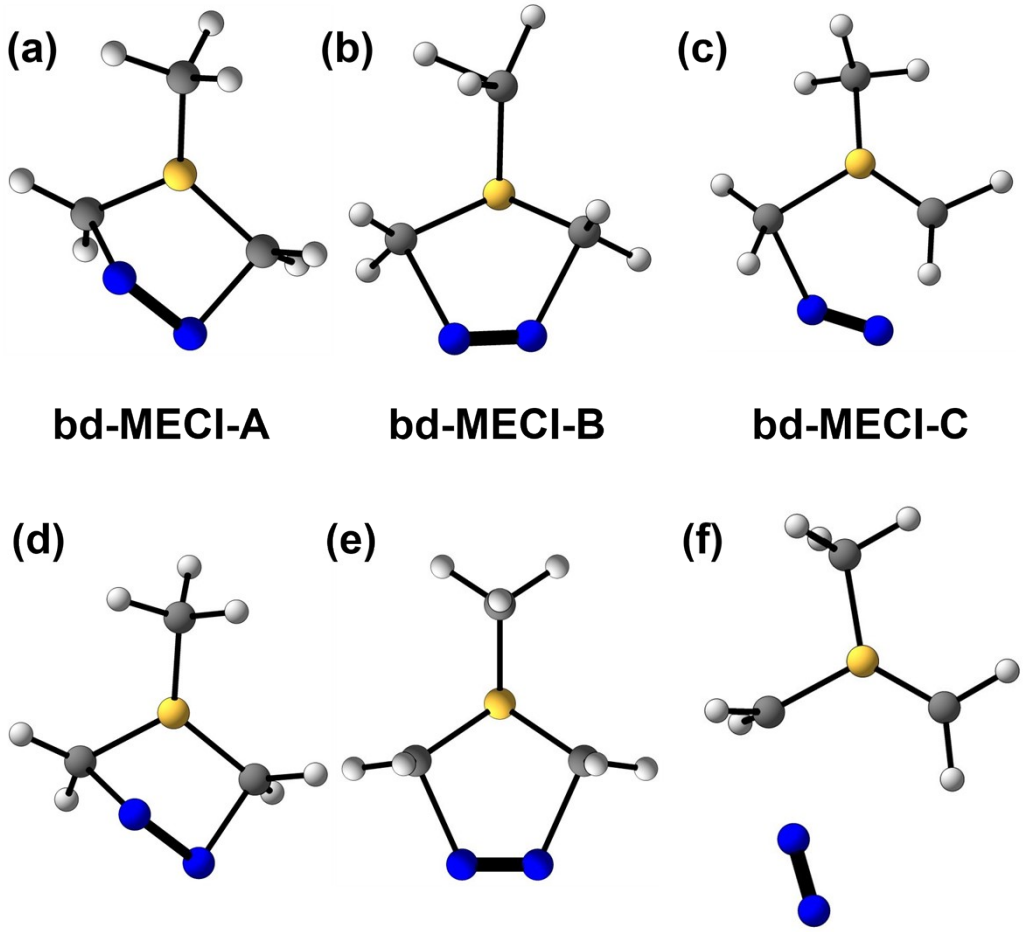

Figure S7. (a-c) Representative geometries of S_1/S_0 hopping points that had (a) a partially π_{NN} isomerized, (b) a pyramidilized boron, and (c) a CN bond broken. These were optimized towards minimum-energy conical intersections using SA5-CASSCF(12,11)/cc-pVDZ. (d-f) The corresponding optimized MECIs: (d) **bd-MECI-A**, (e) **bd-MECI-B**, and (f) **bd-MECI-C**, respectively.

Table S1. SA5-CASSCF(12,11)/cc-pVDZ energies of the optimized MECIs, we optimized three MECIs per commonly encountered S_1/S_0 hopping point geometries containing a partial π_{NN} isomerization, a pyramidalized boron atom, and one broken C-N bond. All energies are presented in eV.

MECI	Geometry Type	RASSCF (eV)
new-traj126-meci	Boron Pyramidalization	3.898755785
new-traj21-meci	Boron Pyramidalization	3.898772928
new-traj207-meci	Denitrogenated	2.672576087
new-bd-traj97-meci	Denitrogenated	2.672603842
new-bd-traj73-meci	πNN isomerization	3.224973493
new-bd-traj9-meci	πNN isomerization	3.224901927

We found that the MECIs optimized from the partially π_{NN} isomerized **bd** geometry were, on average, 3.22 eV above **bd-S$_0$**. There was no significant difference between the optimized MECIs and the initial-guess geometries (*i.e.,* the partial *trans*-π_{NN} was retained). MECIs optimized from geometries with pyramidalized boron were, on average, 3.90 eV above **bd-S$_0$**. These optimized MECIs retained the pyramidalized boron present in the initial guess geometry. These results show that MECIs with partial π_{NN} isomerization are, on average, 0.68 eV lower than MECIs with pyramidalized boron. This aligns with the data presented in Figure S6. The consistent results from individual MECI optimizations across different geometries suggest that the geometries in Figure S6 are not isolated findings but rather part of a systematic pattern.

The last MECI geometry we optimized was **bd-MECI-C**, which started from an initial guess with one broken CN bond (Figure S7f). We hypothesize that the initial cleavage of one CN bond in the excited state directs the trajectory toward an S_1/S_0 hopping point. This results in stepwise N_2 extrusion, starting in the S_1 state and terminating on the S_0 surface. Therefore, we hypothesize that the MECI, optimized from the geometry in Figure S7c, will retain one CN bond. However, MECIs optimized from geometries with one CN bond broken converged to completely dissociated products (*i.e.,* 1,3-diyl and N_2; Figure S7f). This finding suggests that denitrogenation occurs either entirely in the S_1 state or on the ground state, rather than through a stepwise N_2 extrusion process (*i.e.,* one CN cleaves on the S_1 surface and the second CN on the S_0 state).

Thermal rearrangement of the diazoborete, 7

To examine the ground-state rearrangement of the diazoborete reactive intermediate (**7**), we applied density functional theory. Our QM-NAMD ensemble shows that **7** experiences a structural change resulting in **9**. The reaction coordinate diagram is summarized in Figure S8.

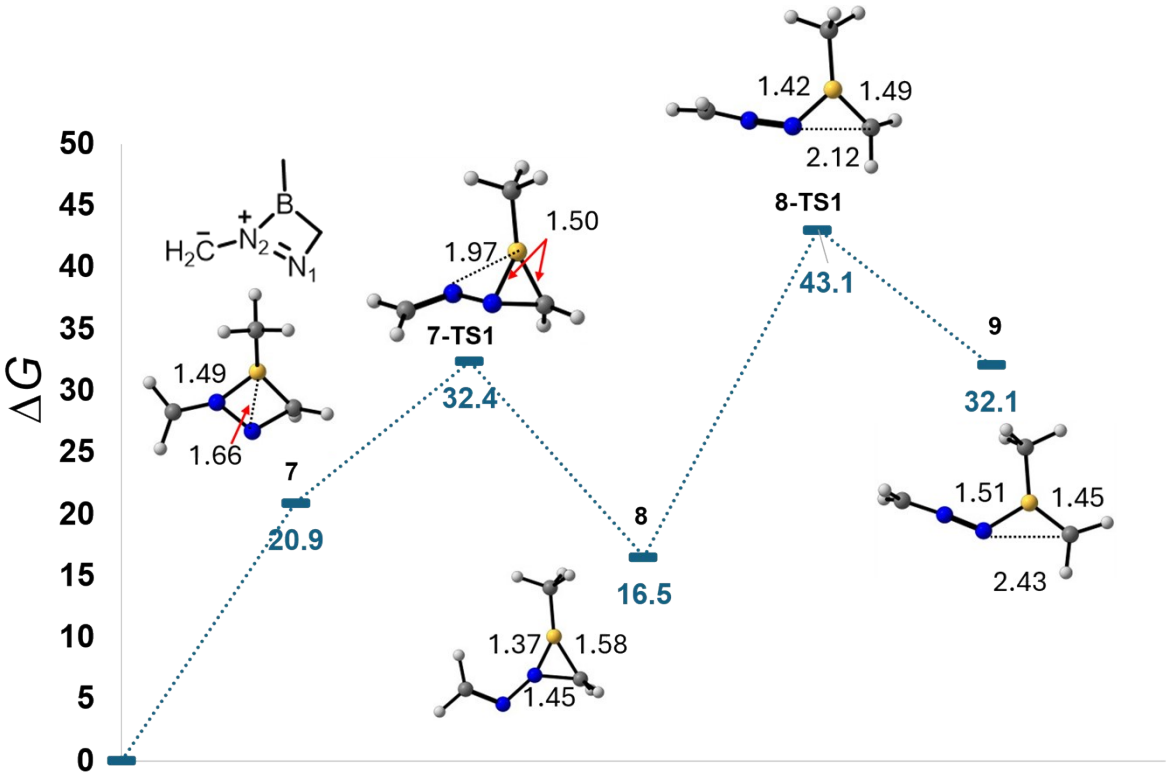

Figure S8. PBE0/6-311+G(d,p) IEFPCM^{water} reaction coordinate diagram of **7** towards **9**. All energies in kcal mol^{-1} are relative to the ground-state optimized borodiazene, **bd-S$_0$**.

Our calculations indicate that diazoborete, **7**, is 20.9 kcal mol^{-1} above the **bd-S$_0$**. This high ΔG (20.9 kcal mol^{-1}) stems from the puckered four-member ring of **7**, which we attribute to a Lewis acid/base interaction between boron and the opposite nitrogen, N_1. We measured the distance between boron and the opposite nitrogen, d_{BN1}, as 1.66 Å, and the distance to the adjacent nitrogen, d_{BN2}, as 1.49 Å in **7**. We identified a transition-state structure, **7-TS1**, that is 32.4 kcal mol^{-1} above **bd-S$_0$**, and has an activation free energy barrier ($\Delta G^{\ddagger}$) of 16.5 kcal mol^{-1}. At **7-TS1**, d_{BN1} and d_{BN2} are measured at 1.97 Å and 1.50 Å, respectively. This reflects a 0.48 Å increase in d_{BN1} and a 0.16 Å decrease in d_{BN2}, signifying a 1,2-rearrangement in which a bond forms between B and N_1, while the BN_2 bond is broken. **7-TS1** leads to **8**, a three-membered ring, with a ΔG of 16.5 kcal mol^{-1} above the **bd-S$_0$**. We no longer measure d_{BN1} at **8**, as this bond has completely broken; instead, we measured all the bonds within the three-membered ring: d_{BN2}, d_{CN2}, and d_{BC}. We measured d_{BN2}, d_{CN2}, and d_{BC} at **7-TS1** to be 1.50 Å, 1.53 Å, and 1.50 Å, respectively, and at **8** to be 1.37 Å, 1.45 Å, and 1.58 Å, respectively. Based on these measurements, we report decreases of 0.13 Å and 0.08 Å for d_{BN2} and d_{CN2}, respectively, and an increase of 0.08 Å in d_{BC} from **7-TS1** to **8**. The significant decrease in d_{BN2} indicates the formation of a bond between B and N_2. Concurrently, the increase in d_{CN2} and the reduction in d_{BC} bonds imply that both bonds adopt their respective optimal single bond lengths in **8**. We did not observe **8** in the QM-NAMD trajectories; rather, it underwent further rearrangement towards **9**. Based on this observation, we optimized a transition state, **8-TS1**, that connects **8** and **9** via a ring-opening where the C-N_1 bond breaks; it has a $\Delta G^{\ddagger}$ of 26.6 kcal mol^{-1}. At **8-TS1**, the measurements for d_{BN2}, d_{CN2}, and d_{BC} were 1.42 Å, 2.12 Å, and 1.49 Å, respectively. This reflected increases of 0.05 Å in d_{BN2} and 0.67 Å in d_{CN2}, along with a decrease of 0.09 Å in d_{BC}. These results indicate that the BN_2 bond has single-bond character at **8-TS1**, while the BC bond experiences complete cleavage. **8-TS1** leads to **9**, which

has a ΔG of 32.1 kcal mol^{-1} relative to **bd-S$_0$.** At **9** d_{BN2}, d_{CN2}, and d_{BC} were measured at 1.52 Å, 2.53 Å, and 1.45 Å, respectively. This demonstrates increases of 0.10 Å and 0.41 Å for d_{BN2} and d_{CN2}, respectively, and a decrease of 0.04 Å at d_{BC}. As such, the BN_2 bond adopts single-bond character, whereas the BC bond adopts double-bond character, resulting in **9** being zwitterionic. We attribute the high ΔG of 9 to this zwitterionic character. Due to the high activation barrier of **8-TS1** (26.6 kcal mol^{-1}) and high ΔG of **9** (32.1 kcal mol^{-1}), we consider compound **8** as a thermal sink for this rearrangement. The presence of **9** in our QM-NAMD trajectories is attributed to the excess vibrational energy after the S_1/S_0 hopping points.